A new relationship on transport properties of nanofluids. Evidence with novel magnesium oxide based *n*-tetradecane nanodispersions

Jose I. Prado [a], Javier P. Vallejo [b], Luis Lugo [a,*]

[a] *CINBIO, Universidade de Vigo, Grupo GAME, Departamento de Física Aplicada, 36310 Vigo, Spain*
[b] *Centro Universitario de la Defensa en la Escuela Naval Militar, Plaza de España s/n, 36920 Marín, Spain*

ARTICLE INFO

ABSTRACT

The worldwide increasing of thermal energy consumption fosters new technological solutions based on nanomaterials. The use of nanofluids enhances energy efficiency leading to eco-friendlier devices. Thus, researchers are encouraged to understand how modified thermophysical properties improve heat transfer capability. Magnesium oxide based *n*-tetradecane nanofluids are designed in terms of stability for cold storage application. Thermal conductivity, viscosity, density, and isobaric heat capacity were determined by transient hot wire, rotational rheometry, mechanical oscillation U-tube, and differential scanning calorimetry. Furthermore, a useful relationship on thermal conductivity and viscosity of nanofluids is proposed based on Andrade, Osida and Mohanty theories. Its reliability is checked with the here reported results and literature data of different nanofluids: titanium oxide within water, silver within poly(ethylene glycol), and aluminium oxide within (1-ethyl-3-methylimidazolium methanesulfonate + water). Similar trends have been found for all nanofluids excepting titanium oxide aqueous nanofluids, this differentiated behaviour being expected by the proposed relationship.

1. Introduction

Formulating a correct pathway to slow down or even mitigate the global warming is a critical political, social, and scientific challenge for the 21st century. There are still many open questions concerning the impacts that policymakers' decisions could cause in the environment [1,2]. In December 2015, the United Nations Framework Convention on Climate Change adopted a new agreement to combat climate change, which legally binds the goal of achieving a global mean temperature increase below 2 K in 2100 comparing to preindustrial levels [3,4]. The Intergovernmental Panel on Climate Change stated in its Fifth Assessment Report that every possible mitigation pathway within the 2 °C objective may require substantial emissions reductions in the coming decades [1]. The development of new and more efficient energy technologies around the world is necessary [5] to achieve this goal. As an example, in 2010 EU policy introduced the Energy Performance of Buildings Directive [6], new and old refurbished buildings having to fulfil the requirements for being considered as "near zero-energy buildings". In this environmental and policy context, Thermal Energy Storage (TES) systems are postulated as very convenient alternatives for meeting the EU energy efficiency objectives, due to their ability to decouple energy production and consumption.

Heating and cooling involves half of the EU energy consumption [7]. Nowadays, cooling sector is a small share of the energy use but the demand is increasing, related to climate change and rising temperatures. Cold TES systems allow energy saving by reducing electricity peak load, i.e., storing cooling capacity (or cold, for simplicity) during off-peak hours and using it during hours of high cold demand [8]. The general performance of such systems are characterized by three sequential processes: charging, storing and discharging [9]. During the charging process, the available cold energy is transferred to the storage medium for accumulation. Cold TES provides large amounts of cold energy in applications where the system has a considerable demand such as air conditioning [10].

Among the different possible manners to store energy within a material, latent heat is the most advantageous way due to the larger storage capacities compared to sensible heat or thermochemical based systems [11]. The materials employed in latent heat TES applications are the so-called Phase Change Materials (PCMs), which are characterized by experimenting a phase transition within the operational temperature range [12]. Considering the variety of these transitions, solid-liquid are the most appropriate due to their tiny volume and pressure variations during phase change transition and to their acceptable latent heats reported. An important issue concerning PCMs is their poor thermophysical profile that leads to lower heat transfer characteristics, causing longer charging-discharging times. These properties, especially thermal conductivity [13,14], could be improved by dispersing

---

* Corresponding author.
E-mail address: luis.lugo@uvigo.es (L. Lugo).

Nomenclature

a	adjustable coefficients in Eq. 4
A	coefficient in Eq. 25
b_0	adjustable coefficients in Eq. 12 (g cm^{-3})
b_1	adjustable coefficients in Eq. 12 (g cm^{-3} K^{-1})
b_2	adjustable coefficients in Eq. 12 (g cm^{-3} K^{-2})
B	coefficient in Eq. 25 (g mol^{-1})
c	adjustable coefficients in Eq. 17
c_p	isobaric heat capacity (J g^{-1} K^{-1})
D_T	fragility strength coefficient (K)
k	Boltzmann's constant (1.380649×10^{-23} J K^{-1})
l	arbitrary distance smaller than σ (m)
m	mass (kg)
M	molecular weight (g mol^{-1})
N	Avogadro's number ($6.02214076 \times 10^{23}$ mol^{-1})
$\dot{q}$	heat power (W)
r_0	radium of the wire (m)
R^2	coefficient of determination
s	standard deviation
t	time (s)
T	temperature (K)
T_0	Vogel divergence temperature (K)
u	adjustable coefficient in Eq. 3 (g cm^{-3} s^{-2})
v	adjustable coefficient in Eq. 3 (g cm^{-3})
x	mole fraction

Greek symbols

α	thermal diffusivity (m^2 s^{-1})
β	adjustable coefficient of κ factor
γ	Euler's constant
$\dot{\gamma}$	shear rate (s^{-1})
Δ	parameter for Bruggeman model, Eqs. 7–8
η	viscosity (mPa s)
η_0	viscosity at infinite temperature (mPa s)
θ	angle between the direction of the motion and that of the heat flow (rad)
κ	factor for Yamada and Ota correlation, Eq. 10
λ	thermal conductivity (W m^{-1} K^{-1})
ν	vibration frequency (s^{-1})
ρ	density (g cm^{-3})
σ	average distance between centre of molecules (m)
τ	period of oscillation (s)
ϕ	fraction of nanoparticles
ψ	adjustable coefficient of κ factor

Abbreviations

AAD%	Absolute Average Deviation
DLS	Dynamic Light Scattering
DSC	Differential Scanning Calorimetry
EDS	Energy-Dispersive X-ray Spectroscopy
HRTEM	High Resolution Transmission Electron Microscopy
NePCM	Nanoenhanced Phase Change Material
NR	Nanofluid Ratio
PCM	Phase Change Material
SAED	Selected Area Electron Diffraction
SEM	Scanning Electron Microscopy
TEM	Transmission Electron Microscopy
TES	Thermal Energy Storage
THW	Transient Hot Wire
TMDSC	Temperature Modulated Differential Scanning Calorimetry
VFT	Vogel-Fulcher-Tammann

Subscripts

bf	base fluid
m	mass fraction
max	maximum
nf	nanofluid
np	nanoparticle
v	volume fraction

nanoscale materials in the PCMs, in such a case Nanoenhanced Phase Change Materials (NePCMs) are mentioned [15,16]. Recently, Ali [17] proposed the use of new NePCMs based on graphene oxide dispersed in RT-35HC at low concentrations, 0.003 and 0.006 wt%, for their use in heat sink for passive cooling of electronic components. Peak temperature of the sink along with charging-discharging time were considerably improved, obtaining maximum reductions of the peak temperature of 32.95 and 37.54% and maximum charging time reductions of 5.4 and 5.6 times that of the empty sink at 0.003 and 0.006 wt % graphene oxide loadings, respectively.

Among the wide variety of possible PCM to use in TES systems, n-alkanes have high latent heat, as well as tiny or null subcooling [11]. Their main disadvantage is the reduced thermal conductivity which can be enhanced by dispersing nanomaterials as previously commented [18]. Taking into account the operating temperatures for cold TES, n-tetradecane arises as a suitable candidate for such systems [19]. To our knowledge, the only approach in the literature of n-tetradecane based nanostructured fluids for cold TES is the study by Jiang et al. [19]. They studied the thermal conductivity of dispersions of CuO nanoparticles in n-tetradecane, obtaining larger enhancements comparing with nanofluids based on the same nanoparticles. They also analysed the differentiated impact of Brownian movement on thermal conductivity enhancements.

In this study, n-tetradecane (n-C$_{14}$) based colloidal fluids using MgO nanoparticles as dispersed nanoscale materials are proposed for use in cold TES. MgO/n-C$_{14}$ have good stability in terms of the temporal evolution of the apparent size. We reported a thermophysical characterization of these nanofluids, determining their thermal conductivity, viscosity, density, isobaric heat capacity, and thermal diffusivity. These properties were also compared with different predicting equations and correlations.

In the early XX century, there were several attempts to apply kinetic theory of gases to liquids [20–22] without clear agreement with experimental results [23]. As it is well known, Andrade [24] developed a theory of the viscosity of liquids based on simple classical approaches without considering any quantum interpretation which it would not introduce substantial modifications in the results [25]. He supposed that a theory of liquids should be approached from the point of view of solid state instead of from the kinetic theory of gases [24], because the distances between molecules are more solid-like and also, consequently, intermolecular forces are not very different [26]. Andrade stated that the main difference between a liquid and a solid from a molecular perspective is that the amplitude of the molecular motion in the former is so large so molecules may collide with each other. Similar to Andrade's theory of the viscosity of liquids, Osida [27] presented a model for the thermal conductivity of dielectric liquids for which the electronic part of heat transport is negligible. He assumed that in the presence of a temperature gradient, the heat is exchanged when molecules collide due to their vibration, transferring their translational and rotational energy. Mohanty [28] carried out a relationship between thermal conductivity and viscosity of liquids based on the theoretical results by Andrade and Osida. He suggested a modification of this equation taking into account an examination of this relation for a few number of liquids, assuming that it must require correction. Accordingly, here we develop a new understanding on the relevant transport properties of nanofluids for heat transfer applications from previous works on molecular [24,27,28] and ionic liquids [29]. This suggested relationship on transport properties for nanostructured fluids was analysed for MgO/n-tetradecane nanodispersions along with available literature data for Ag/PEG400 [30], TiO$_2$/H$_2$O [31], and Al$_2$O$_3$/([C$_2$mim][CH$_3$SO$_3$]:H$_2$O) [32,33] nanofluid sets.

Therefore, the main objective of the present study is twofold: (i) to elaborate and thoroughly characterized new nanofluids based on colloidal dispersions of MgO nanoparticles in *n*-tetradecane for their use in cold energy storage applications and (ii) to propose an empirical model that relates transport properties of nanofluids to understand the effect of reported enhancements in the heat transfer performance. This analysis is here proposed for the first time as a useful tool from transport properties that could contribute towards the design of new nanofluids for thermal energy applications.

2. Experimental

2.1. Materials

MgO nanoparticles were provided by IoLiTec (Heilbronn, Germany) with a mass purity of 99.9%, a bulk density of 3.60 g cm^{-3}, and an average size of 35 nm, according to the supplier. The base fluid, *n*-tetradecane or *n*-C$_{14}$, was purchased from Alfa Aesar (Haverhill, USA) with a mass purity of 99%, a melting point around 279.15 K, a flash point of 372.15 K, and a boiling point of 525.15–527.15 K. In this study, Sorbitan monooleate, Span® 80, purchased from Sigma-Aldrich (St. Louis, USA) with a density of 0.986 g cm^{-3}, was used as a surfactant. Toluene with a mass purity of 99.8% was supplied by Sigma-Aldrich (Saint Louis, USA). Milli Q-Grade water was produced by means of a Millipore system (Billerica MA, USA), with 18.2 MΩ cm at 298 K. All reagents were used without performing any additional purification and were weighted in an analytical balance Sartorius model CPA225 (Göttingen, Germany) with an uncertainty of $1 \cdot 10^{-5}$ g.

2.2. Nanofluids preparation

A two-step method was used to prepare the nanofluids. The nanopowder was weighted and then stirred into a predetermined volume of the base fluid by means of a VELP Scientifica ZX3 Advanced Vortex Mixer (Usmate, Italy). After that, samples were dispersed in an ultrasonic homogenizer Bandelin Sonopuls HD 2200 (Berlin, Germany) with an operating frequency of 20 kHz for 30 min. In this study, nanofluids were elaborated at nanoparticle mass fractions, ϕ_m, of 1.0, 2.5, 5.0, and 10.0 wt% which corresponds to 0.21, 0.54, 1.1, and 2.3 vol% volumetric fractions, ϕ_v, and to 0.047, 0.11, 0.21, and 0.35 mol fractions, x_{np}, respectively. To calculate the volumetric fractions, a density for MgO nanoparticles of 3.58 g cm^{-3} was used [34] in the following equation:

$$\frac{1}{\phi_v} = 1 + \frac{1-\phi_m}{\phi_m} \frac{\rho_{np}}{\rho_{bf}} \tag{1}$$

where ρ stands for the density whereas 'np' and 'bf' subscripts refer to nanopowder and base fluid, respectively. Li et al. [35] reported the stability enhancement of *n*-alkanes nanofluids containing CuO nanoparticles when oleates are used as dispersants. Likewise, the goodness of the use of Span® 80 as surfactant in *n*-C$_{14}$ dispersions was reported by Jiang et al. [19]. In order to guarantee the stability of the dispersions, Span® 80 in a 1:1 mass proportion with the nanoparticles was also used as a surfactant before stirring and dispersing. In this work, MgO/*n*-C$_{14}$ is the notation for referencing the nanostructured fluids elaborated as above-mentioned, i.e., MgO dispersed within *n*-C$_{14}$ and containing Span® 80 in a 1:1 nanoparticles:surfactant mass proportion.

2.3. Experimental methods

EDS analysis was conducted by using a field emission gun Scanning Electron Microscope, SEM, model JEOL JSM-6700F (JEOL, Tokyo, Japan) working at an accelerator voltage of 10 kV in backscattering electron image (Yttrium Aluminium Garnet type detector). Samples were prepared by depositing a drop of MgO dispersed in analytical grade methanol on the top of a silica support covered with a thin layer of carbon and dried under atmospheric conditions.

The size and morphology of the dry nanopowder were studied through Transmission Electron Microscopy (TEM) and High Resolution Transmission Electron Microscopy (HRTEM) analyses were conducted on a JEOL JEM-1010 (Tokyo, Japan) and a field emission JEOL JEM-2010 FEG, operating at acceleration voltages of 100 kV and 200 kV, respectively. Moreover, the crystalline structure of MgO nanoparticles was analysed from the diffraction patterns obtained by means of the Selected Area Electron Diffraction (SAED) technique. Samples were prepared by depositing a single drop of MgO diluted dispersion in analytical grade 1-butanol on the top of a 400-mesh cupper grid covered with formvar and coated with carbon.

Colloidal stability was evaluated using the Dynamic Light Scattering (DLS) technique by means of a Zetasizer Nano ZS (Malvern Instruments, Malvern, UK) operating at 298.15 K with a scattering angle of 173°. Samples introduced inside poly(methyl methacrylate) cuvettes are lighted by a He—Ne laser with a beam wavelength of 632.8 nm and a maximum power of 4 mW. Light scattering due to the Brownian motion of the particles dispersed in the fluid is detected and related to their hydrodynamic diameter. Two samples of MgO/*n*-C$_{14}$ 1 wt% were used in two different measuring cells to analyse their size distributions over 30 days. One of the samples was remained in static conditions and the other one was mechanically shaken by means of a ZX3 Advanced Vortex Mixer (VELP Scientifica, Usmate, Italy) for more than 1 h before each measurement [36].

Thermal conductivities of base fluid and MgO/*n*-C$_{14}$ samples were measured within the temperature range from 283.15 K to 333.15 K by using a THW-L2 (Thermtest, Fredericton, Canada) thermal conductivity meter. An EchoTerm Dry Bath (Torrey Pines Scientific, West Carlsbad, USA) was coupled to the device to remain the sample at constant temperature. The apparatus is based on the transient hot wire (THW) method in which thermal conductivity is determined by means of a non-steady state heat transfer process initiated by a constant power that heats a sensor wire. Thus, thermal conductivity can be obtained from the slope of the temperature evolution, by using the following Eq. [37]:

$$\lambda(T) = \frac{\dot{q}}{4\pi \Delta T} \ln\left(\frac{4\alpha t}{r_0^2 e^\gamma}\right) \tag{2}$$

where λ, $\dot{q}$, ΔT, α, t, r_0, and γ stand for the thermal conductivity of the fluid, the heat supplied by the wire, the temperature rise of the fluid, the thermal diffusivity of the fluid, the test time, the radium of the wire, and the Euler's constant, respectively.

The sensor consists of a 60 mm thin heating wire joined to a printed circuit board covered with a slim layer of Kapton. Samples were poured into the sample holder and the sensor was vertically placed. This device allows to perform measurements in accordance with ASTM D7896–19. The expanded thermal conductivity uncertainty is estimated to be below 5%.

The rheological behaviour of proposed nanofluids was studied in a Physica MCR 101 rheometer (Anton Paar, Graz, Austria) with a cone-plate geometry of 1° cone angle and 50-mm diameter. This rheometer allows controlling torques from 0.1 µN m to 200 mN m. The sample temperature was regulated in the range between 293.15 K and 343.15 K, every 10 K, by using a Peltier plate. The expanded viscosity uncertainty was estimated to be better than 5% [38].

Density of samples was obtained by means of a DMA 500 density meter (Anton Paar, Graz, Austria), using the oscillating U-tube technique, which relates the resonant frequency of the tube with the density of the sample, according to the following equation:

$$\rho(T) = u(T)\tau^2 - v(T) \tag{3}$$

where τ is the period of the oscillation. The characteristic coefficients $u(T)$ and $v(T)$ can be determined by performing measurements of oscillation period in the required temperature range of at least two reference substances whose density is reported in the literature. In this study, Milli Q-Grade water [39] and toluene [40] were used as well-known substance to perform a density calibration every 5 K in the temperature range from 288.15 K to 313.15 K. The estimated density expanded uncertainty was declared below 0.1% [32,41].

Isobaric heat capacities of the base fluid were experimentally determined in a heat-flux Differential Scanning Calorimeter (DSC) Q2000 (TA Instruments, New Castle, USA), equipped with a refrigerated cooling system RSC9, from 283.15 K to 333.15 K. A quasi-isothermal Temperature Modulated Differential Scanning Calorimeter (TMDSC) method was employed [42] and results were interpreted by using Universal Analysis 2000 software (V4.5A) from TA Instruments. The expanded heat capacity uncertainty was estimated to be better than 3% overall the entire temperature range [43]. Isobaric heat capacity data for MgO nanoparticles was obtained from a previous study by Cabaleiro et al. [42].

3. Results and discussion

3.1. Nanopowder characterization

The elemental analysis of MgO nanopowder demonstrates the presence of Mg (18.66 at.%) and O (14.08 at.%), corresponding to the stoichiometric ratio of MgO compound, as well as Si (64.09 at.%) and C (3.17 at.%), corresponding to the support material and the coating of the sample for EDS analysis, respectively.

Furthermore, a complete TEM characterization of the studied nanoparticles is enclosed in Fig. 1. Herein, Fig. 1a shows a pseudo-spherical shape and a certain level of polydispersity. A histogram with the size distribution of MgO nanoparticles (Fig. 1b) was constructed from TEM images (more than 200 nanoparticles), obtaining a mean particle size of (45 ± 3) nm and a polydispersity index of 0.32, assuming a log-normal distribution function [44]. Fig. 1c encloses a HRTEM image of a single MgO nanoparticle that shows the different layers of the crystalline structure. In Fig. 1d, an interlayer distance of 2.16 Å was measured, corresponding to the d-spacing between (200) planes of MgO [41].

Fig. 1e displays the analysis of the Selected Area Electron Diffraction (SAED) pattern of MgO nanoparticles performed with the CrysTBox software [45], which allows individual rings to be identified and compared with any unit cell. It demonstrates the polycrystalline structure of the nanoparticles, the SAED pattern agreeing with that of MgO [46].

3.2. Stability

The stability of the 1 wt% MgO/n-C$_{14}$ nanofluid containing Span® 80 as surfactant in a 1:1 nanoparticles:surfactant mass ratio was analysed over 30 days. The dispersion under static conditions evolved from a polydisperse sample (bimodal size distribution) to a monodisperse sample (unimodal size distribution) with a narrower peak shifted to the left (less apparent size), as observed in Fig. 2a. All these effects indicate the sedimentation of some aggregates or clusters in static conditions which entails a reduction in the polydispersity and apparent size, as previously discussed [41].

Fig. 2b shows how apparent size of the static dispersion was reducing from the preparation of the sample to the seventh day after that, remaining at a constant value around 200 nm. Instead, shaken sample maintains a quite similar size distribution (Fig. 2a), as well as the mean apparent size (Fig. 2b). Therefore, the potential and feasibility of the explored samples for heat transfer and storage applications is also evidenced from the point of view of the stability challenge in both static and shaken conditions of the dispersions. This issue is relevant by using
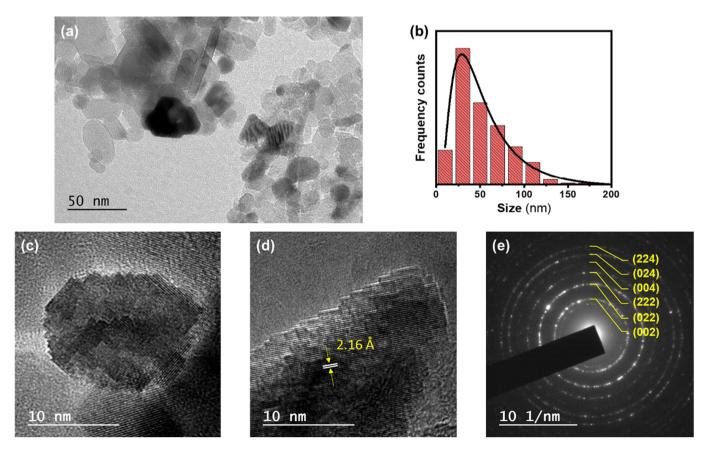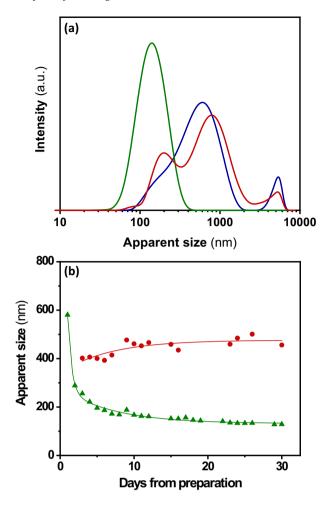

Fig. 1. Characterization of MgO nanoparticles. (a) TEM image. (b) Size distribution. (c and d) HRTEM images. (e) Selected area electron diffraction pattern.
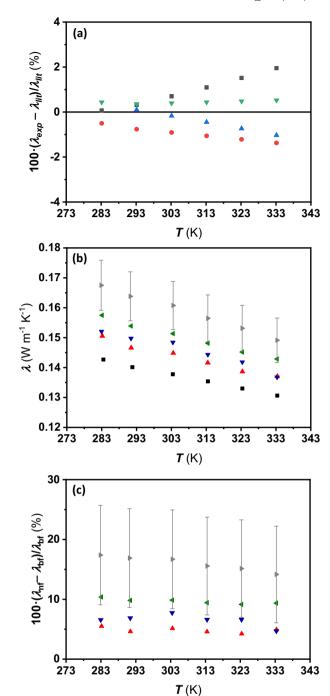
Fig. 2. (a) Nanoparticle size distribution for 1 wt% MgO/n-C$_{14}$ nanofluid: 1st day (—); 30th day static sample (—); and 30th day shaken sample (—). (b) Temporal variation of average apparent size of MgO nanoparticles in the nanofluid: static sample (●) and shaken sample (▲). Lines are used to guide eyes.

this technology, and not always sufficiently addressed in the literature [41,47].

3.3. Thermal conductivity

Firstly, experimental thermal conductivity values of n-C$_{14}$ were compared with those reported in the literature [19,48–50] to check the reliability of the data obtained in this study. As shown in Fig. 3a, average absolute deviations (AADs%) lower than 2% are obtained, which agrees with the combined expanded uncertainties, obtaining superior deviations at higher temperatures.

Dependence and enhancements of the thermal conductivity on temperature for base fluid and MgO/n-C$_{14}$ nanodispersions were depicted in Fig. 3. As can be observed, the higher the mass fraction, the higher the thermal conductivity, the enhancements ranging from 4.2% to 17%. No influence of the temperature on these enhancements is significantly noted for all studied nanostructured fluids, as reported in Fig. 3c. It should be noted that the thermal conductivity of the base fluid changes with temperature, while the solid nanoparticles do not show significant differences of thermal conductivity values in the studied temperature range. Therefore, the temperature dependence of the thermal conductivity of well-dispersed and stable nanofluids behave like those of the base fluid. The obtained thermal conductivity enhancements are slightly higher than those obtained for MgO/PureTemp 8 dispersions [41]; for instance 4.8% for MgO/n-C$_{14}$ versus 3% for MgO/PureTemp 8 dispersions at MgO mass fraction of 1 wt%.

Fig. 3. (a) Relative deviations between experimental n-C$_{14}$ thermal conductivity values of this study and those reported in the literature at different temperatures: Calado et al. [48] (■); Wada et al. [49] (●); Kenisarin [50] (▲); Jiang et al. [19] (▼). Temperature dependence of the (b) thermal conductivity and (c) thermal conductivity enhancement for MgO/n-C$_{14}$ samples at different nanoparticle mass fractions: 0 wt% (■); 1.0 wt% (▲); 2.5 wt% (▼); 5.0 wt% (◄); and 10.0 wt% (►). Error bars indicate the expanded uncertainty (b) and the combined uncertainty (c).

The experimental data were correlated by using the following proposed equation:

$$\frac{\lambda_{nf}}{\lambda_{bf}}(\phi_v) = 1 + a\,\phi_v \qquad (4)$$

where the subscripts 'bf' and 'nf' stand for base fluid and nanofluid and a parameters were determined by means of least squares adjustments for each temperature and are summarized in Table 1.

Table 1

Fitting parameters and standard deviations, s, obtained from Eqs. 4 and 17 for MgO/n-C$_{14}$ samples at different temperatures.

	283.15 K	293.15 K	303.15 K	313.15 K	323.15 K	333.15 K
Eq. 4						
a	8.209	7.946	7.973	7.418	7.219	6.790
$10^2 s$	3.4	3.0	3.7	3.1	3.0	3.1
Eq. 17						
c	0.410	0.393	0.402	0.368	–	–
$10^2 s$	1.1	0.65	0.85	0.57	–	–

Experimental thermal conductivity results were compared with widely used predictive models [51–53] and correlations [54]. As an example, Fig. 4 depicts the experimental relative thermal conductivities along with those results from the different models at 303.15 K. Thermal conductivity data of MgO nanoparticles from Hofmeister [55] was employed for calculations, values ranging from 51.58 to 43.61 W m^{-1} K^{-1} in the temperature range from 283.15 K to 333.15 K.

The first predictive model describing suspensions of spherical nanoparticles into a fluid was developed by Maxwell [51]:
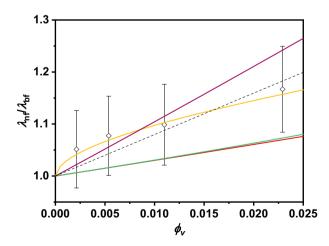
$$\frac{\lambda_{nf}}{\lambda_{bf}} = \frac{\lambda_{np} + 2\lambda_{bf} + 2(\lambda_{np} - \lambda_{bf})\phi_v}{\lambda_{np} + 2\lambda_{bf} - (\lambda_{np} - \lambda_{bf})\phi_v} \qquad (5)$$

in which λ_{np} stands for the thermal conductivity of the nanoparticles. This classical theory only takes into account the amount of dispersed nanoparticles, without considering other effects as shape, pH, aggregation, or Brownian motion. In addition, it is only applicable to low concentrated nanofluids. Bruggeman [52] introduced a similar model that is better suited to spherical nanoparticles, has no limitation for concentration, and also takes into account the effect of clustering. The predictive equation was originally proposed in an implicit form:

$$\phi_v \left(\frac{\lambda_{np} - \lambda_{nf}}{\lambda_{np} + 2\lambda_{nf}} \right) + (1 - \phi_v)\left(\frac{\lambda_{bf} - \lambda_{nf}}{\lambda_{bf} + 2\lambda_{nf}} \right) = 0 \qquad (6)$$

A solution of Eq. 6 was derived by Murshed et al. [56], as follows:

$$\frac{\lambda_{nf}}{\lambda_{bf}} = \frac{1}{4}\left[(3\phi_v - 1)\frac{\lambda_{np}}{\lambda_{bf}} + (2 - 3\phi_v) + \sqrt{\Delta} \right] \qquad (7)$$

where Δ is a parameter that depends on the volume fraction and thermal conductivities of the nanoparticles and the base fluid:

$$\Delta = (3\phi_v - 1)^2 \left(\frac{\lambda_{np}}{\lambda_{bf}} \right)^2 + (2 - 3\phi_v)^2 + 2\left(2 + 9\phi_v - 9\phi_v^2 \right)\left(\frac{\lambda_{np}}{\lambda_{bf}} \right) \qquad (8)$$

Xue [53] presented a modification of the Maxwell model in which uniquely accounts the effect of volume fraction and other factors are neglected:

$$\frac{\lambda_{nf}}{\lambda_{bf}} = \frac{1 - \phi_v + 2\phi_v \frac{\lambda_{np}}{\lambda_{np} - \lambda_{bf}} \ln\left(\frac{\lambda_{np} + \lambda_{bf}}{2\lambda_{bf}} \right)}{1 - \phi_v + 2\phi_v \frac{\lambda_{bf}}{\lambda_{np} - \lambda_{bf}} \ln\left(\frac{\lambda_{np} + \lambda_{bf}}{2\lambda_{bf}} \right)} \qquad (9)$$

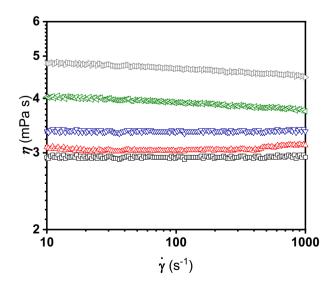Yamada and Ota [54] proposed a semi-empirical correlation based on the unit cell of the nanoparticles, as follows:

$$\frac{\lambda_{nf}}{\lambda_{bf}} = \frac{1 + \kappa\frac{\lambda_{bf}}{\lambda_{np}} + \kappa\left(1 - \frac{\lambda_{bf}}{\lambda_{np}}\right)\phi_v}{1 + \kappa\frac{\lambda_{bf}}{\lambda_{np}} - \left(1 - \frac{\lambda_{bf}}{\lambda_{np}}\right)\phi_v} \qquad (10)$$

where κ is a factor which depends on the shape of the nanoparticles. This κ factor was obtained following the same approach by Yamada and Ota [54] according to the functional form $\kappa = \beta\,\phi_v^{-\psi}$, where $\beta = 0.85$ and $\psi = 0.51$ were optimized by means of a least-squares adjusting method.
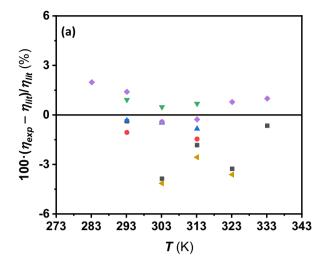
The reliability of the above presented models to predict our experimental data was checked considering all temperatures, obtaining AADs% of 6.1%, 6.0%, and 3.1% for Maxwell, Bruggeman, and Xue, respectively. Maxwell and Bruggeman models underestimate the experimental values, as illustrated in Fig. 4 at 303.15 K. The employed correlation, Eq. 10, leads to obtain the best agreement with our experimental data, with an AAD% of 0.74% for all isotherms, as Fig. 4 also gathers as an example.
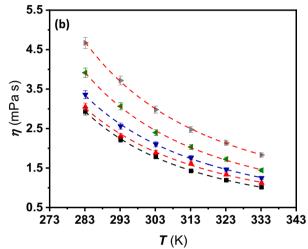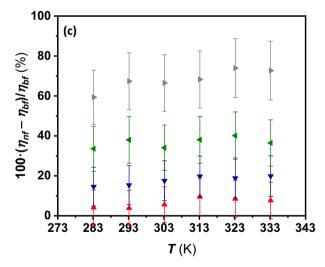
3.4. Rheological behaviour

Rotational tests were performed in an operating shear rate range from 10 s^{-1} to 1000 s^{-1}. Fig. 5 shows the obtained flow curves of the base fluid and nanofluids at 283.15 K, the viscosity remaining constant over the entire shear rate range, even for the highest concentrated nanofluids. This fact evidences Newtonian behaviour for the previously

Fig. 4. Relative thermal conductivity enhancement as a function of nanoparticle volume fraction for MgO/n-C$_{14}$ samples at 303.15 K. Experimental values ($\Diamond$); Eq. 4 (—); Yamada and Ota [54] Eq. 10 (—); Maxwell [51] Eq. 5 (—); Bruggeman [52] Eq. 7 (—); and Xue [53] Eq. 9 (—). Error bars indicate the combined uncertainty.

Fig. 5. Flow curves for MgO/n-C$_{14}$ samples at 283.15 K and volume fractions: 0 vol% ($\square$); 0.21 vol% ($\triangle$); 0.54 wt% ($\triangledown$); 1.1 wt% ($\triangleleft$); and 2.3 wt% ($\triangleright$).

Fig. 6. (a) Comparison between experimental and literature viscosity data for *n*-tetradecane against temperature: Ducoulombier et al. [58] (■); Zhang et al. [59] (●); Liu et al. [60] (▲); Prak et al. [61] (▼); Santos et al. [62] (◆); and Kian et al. [63] (◀). Temperature dependence of the (b) viscosity and (c) increments in viscosity for MgO/*n*-C$_{14}$ samples at volume fractions: 0 vol% (■); 0.21 vol% (▲); 0.54 vol% (▼); 1.1 vol% (◀); and 2.3 vol% (▶). Eq. 11 (—). Error bars indicate the expanded uncertainty (b) and the combined uncertainty (c).

stated conditions. Spherical shape of nanoparticles prevents the formation of large aggregates, which would involve the establishment of a gel network within the fluid, entailing viscoelastic nanofluids. This behaviour agrees with the established knowledge on the rheological performance of dispersions based on spherical nanoparticles and the mentioned good stability of the nanofluids, with lack of aggregation phenomena, as pointed out by Sharma et al. [57].

Experimental shear viscosities belonging to the base fluid *n*-C$_{14}$ at different temperatures are compared with values from the literature [58–63] in Fig. 6a. A good agreement can be observed with an AAD% lower than 4.2% and a Bias of 0.057 mPa s (1.9%), which are lower than the above-mentioned expanded uncertainty.

Fig. 6b shows the evolution of the viscosity over temperature, enclosing the experimental data for the base fluid along with those of the nanofluids at constant shear stress of 0.5 Pa. Dynamic viscosity of MgO/*n*-C$_{14}$ samples exponentially decreases with the temperature (up to 64%) as a consequence of the increasing intermolecular distance within the fluid [33], following the elsewhere reported trend [64]. Dynamic viscosity increases with the loading of nanoparticles reach up to 68% for the 2.3 vol% at 283.15 K (Fig. 6c). These increments are more than twice those found by Żyła [65] for ethylene glycol-based MgO nanofluids, due to a less viscous base fluid fosters higher viscosity increments of the constituted nanofluids, especially at lower temperatures [66].

One of the most widely used equations to model the evolution of viscosity with temperature is the well-known modification of Andrade's equation, commonly named as Vogel-Fulcher-Tammann (VFT) [67–69]:

$$\eta(T) = \eta_0 \exp\left(\frac{D_T}{T-T_0}\right) \tag{11}$$

where η_0 is the viscosity at infinite temperature, D_T is the fragility strength coefficient and T_0 is the Vogel divergence temperature, i.e., a temperature below glass transition at which an ideal glass phase change transition may occur [70]. Table 2 encloses these parameters for each mass fraction, showing a good agreement with standard deviations lower than 0.015 mPa s, as also shown in Fig. 6b.
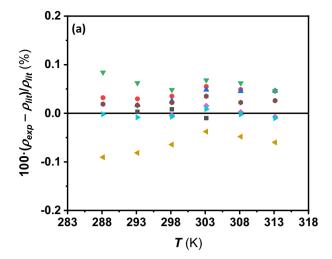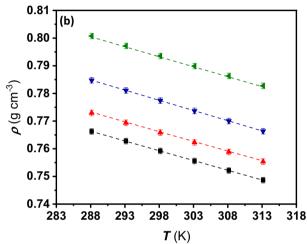
3.5. Density

Prior to measure the prepared nanostructured fluids, a comparison between our experimental values for *n*-C$_{14}$ and literature density data [59,61,62,71–75] was performed, showing AADs% less than 0.1%, as shown in Fig. 7a, which agrees with the corresponding expanded uncertainties, as stated in the section 2.3.
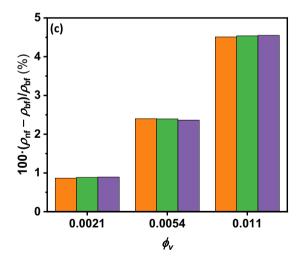
Obtained experimental density values for the dispersions are displayed in Fig. 7b. As generally reported for nanostructured fluids,

Table 2
Fitting parameters and standard deviations of VFT model, Eqs. 11 and 12 for MgO/*n*-C$_{14}$ nanofluids at different volume fractions.

	0 vol%	0.21 vol%	0.54 vol%	1.1 vol%	2.3 vol%
Eq. 11					
η_0 / mPa s	0.05121	0.06404	0.07446	0.09598	0.1501
A / K	246.7	246.6	238.9	221.6	199.7
T_0 / K	142.7	135.7	138.4	127.6	149.5
$10^2 s$ / mPa s	0.52	1.4	1.1	1.3	0.82
Eq. 12					
b_0 / g cm^{-3}	0.9939	1.031	0.9915	1.025	–
$10^3 b_1$ / g cm^{-3} K^{-1}	−0.867	−1.07	−0.700	−0.833	–
$10^7 b_2$ / g cm^{-3} K^{-2}	2.7	6.1	−0.62	1.8	–
$10^4 s$ / g cm^{-3}	0.59	0.16	0.28	0.34	–

Fig. 7. (a) Relative percentage deviations between experimental n-C_{14} density data of this work and those reported by other authors: Camin et al. [71] (■); Johansen et al. [72] (●); Khansanshin et al. [73] (▲); Valencia et al. [74] (▼); Zhang et al. [59] (◆); Kariznovi et al. [75] (◄); Prak et al. [61] (▶); and Santos et al. [62] (●). (b) Temperature dependence of the density of MgO/n-C_{14} samples at mass fractions: 0 wt% (■); 1.0 wt% (▲); 2.5 wt% (▼); and 5.0 wt% (◄). Eq. 12 (—). Error bars indicate the expanded uncertainty. (c) Nanofluid density improvements over volumetric fraction in relation to the base fluid at: 293.15 K (■); 303.15 K (■); and 313.15 K (■).

density is higher when nanoparticle volume fraction is increased. In this case, an increment up to 4.5% is reached at a volume fraction of 1.1 vol%.

Experimental density data of each fluid was correlated according with a second-order polynomial adjustment:

$$\rho(T) = b_0 + b_1 T + b_2 T^2 \tag{12}$$

where b_i parameters were determined by means of least squares adjustments and are summarized in Table 2. Experimental density values were compared with those predicted by the mixing-based equations for the volume fraction [76] and the mass fraction [77]:

$$\rho_{nf} = \phi_v \rho_{np} + (1-\phi_v)\rho_{bf} \tag{13}$$

$$\frac{1}{\rho_{nf}} = \frac{\phi_m}{\rho_{np}} + \frac{1-\phi_m}{\rho_{bf}} \tag{14}$$

The value for the density of MgO nanoparticles employed in Eqs. (13) and (14) was 3.579 g cm^{-3} [34]. The agreement between our experimental and predicted data shows AADs% of 0.46% and 1.0% and a maximum deviation of 1.2% and 1.9%, respectively. These AADs% from Eq. 13 are 0.16% higher than those obtained using the same equation than Marcos et al. [77] for PEG 400-based functionalized graphene nanoplatelets dispersions.

3.6. Isobaric heat capacity

Firstly, a comparison between the experimental values of isobaric heat capacity of n-C_{14} and those obtained from the literature [73,78–80] is shown in Fig. 8a against temperature. An AAD% lower than 0.5% was obtained over the wide temperature range. Therefore, these deviations are within the estimated expanded uncertainty for the experimental determination of c_p, as above-mentioned.

To compute the c_p values of the designed MgO/n-C_{14} samples, the Raud et al. [81] correlation, one of the most trustful equation to this purpose [33], was used:

$$c_{p,nf}(T) = \phi_m \cdot c_{p,np}(T) + (1-\phi_m) \cdot c_{p,bf}(T) \tag{15}$$

where $c_{p,nf}$, $c_{p,np}$, and $c_{p,bf}$ stand for the isobaric heat capacity of nanofluid, nanoparticles and base fluid, respectively. The use of Eq. 15 is justified from the point of view of the involved uncertainties and mass concentration dependence, following the conclusions obtained by Cherecheş et al. [33]. Accordingly, the c_p-temperature dependence for all the nanofluids in Fig. 8b is similar than that of the base fluid, c_p values incrementing 6.7% over the analysed temperature range. In addition, isobaric heat capacity values decrease with increasing nanoparticle loading and these reported diminutions are lower than 6% in the whole studied mass fraction range, as can be seen in Fig. 8c.

These reductions are in agreement with the usual trends reported in the literature [33,42], the higher the mass fraction, the lower the isobaric heat capacity. This fact can be directly explained in terms of the mixing theory, since the c_p of MgO nanoparticles is lower than the c_p of n-tetradecane throughout the entire temperature range. Therefore, the c_p of the gathered nanofluids are consequently lower than those of the base fluid. Cabaleiro et al. [42] obtained similar diminution in c_p, up to 9%, for ethylene glycol-based MgO nanofluids at 15 wt%. Therefore, even if the dispersion of nanoparticles into the base fluid contributes to decrease c_p values, reported reductions are very tiny, so the impact on the behaviour of the proposed nanofluids will have not an
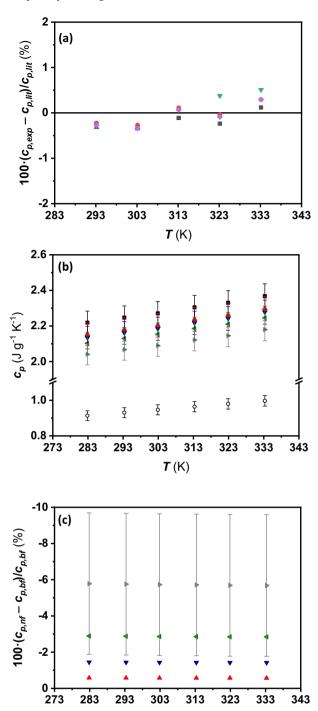
Fig. 8. (a) Relative deviations between experimental isobaric heat capacity values of n-C$_{14}$ in this study and those reported by: Benson et al. [78] (■); Khasanshin and Shchemelev [73] (●); Pardo et al. [79] (▲); and Regueira et al. [80] (▼). (b) Isobaric heat capacities and (c) reductions in c_p vs. temperature of MgO/n-C$_{14}$ samples at mass fractions: 0 wt% (■); 1.0 wt% (▲); 2.5 wt% (▼); 5.0 wt% (◀); and 10.0 wt% (▶). c_p values of MgO nanoparticles (○).[40] Error bars indicate the expanded uncertainty (b) and the combined uncertainty (c).

important influence on their heat transfer behaviour. The noticeable reduced c_p values of MgO nanoparticles compared to those of the base fluid entail this effect. As regards to the reductions in c_p for the nanostructured fluids, it is remarkable the practically non temperature-dependence for each different loaded sample (Fig. 8c).
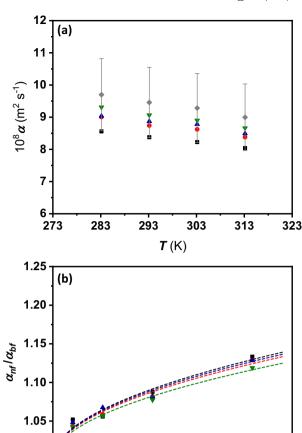

Fig. 9. (a) Thermal diffusivity of MgO/n-C$_{14}$ samples as a function of temperature at mass fractions: 1 wt% (■); 2.5 wt% (●); 5 wt% (▲); and 10 wt% (▼). Error bars indicate the combined uncertainty. (b) Relative thermal diffusivity enhancement of MgO/n-C$_{14}$ samples against mass fraction at temperatures: 283.15 K (■); 293.15 K (●); 303.15 K (▲); and 313.15 K (▼). Eq. 17 (—).

3.7. Thermal diffusivity

A useful analysis to estimate the thermal performance of a nanofluid in thermal energy storage applications is by means of the thermal diffusivity, α. This thermophysical property is related to the capacity of any material to transfer energy stored within it. It can be easily computed from density, ρ, thermal conductivity, λ, and isobaric heat capacity, c_p, values as follows:

$$\alpha = \frac{\lambda}{\rho c_p} \tag{16}$$

In this study, thermal diffusivities were obtained from data here reported in the temperature range from 283.15 K to 313.15 K and results were plotted in Fig. 9. Thermal diffusivity of the gathered nanofluids decreases with temperature (Fig. 9a) in a similar way than the base fluid, with 7% reductions in the studied temperature range. This behaviour is due to the fact that as temperature increases heat conduction gets reduced by the augmentation of the separation between nanoparticles whereas the higher the temperature, the higher the isobaric heat capacity. Therefore, the resulting thermal diffusivity is reduced with increasing temperature. The observed enhancements of the thermal diffusivities with mass fraction are non-temperature dependent,

because of the same effect for thermal conductivity, density and isobaric heat capacity. A maximum 13% improvement is reached at 10 wt% (Fig. 9b). In addition, it must be noted that the α-enhancement within the studied mass fraction range follows a root function tendency.

Accordingly, the following least squares adjustment in nanoparticle mass fraction was used to correlate the experimental values of thermal diffusivity:

$$\frac{\alpha_{nf}}{\alpha_{bf}}(\phi_m) = 1 + c\,\phi_m^{\,0.5} \tag{17}$$

where c are adjustable parameters, whose obtained values are enclosed in Table 1 along with the standard deviation of the correlations. The dependence of the thermal diffusivity enhancement with the mass fraction in the range from 1 wt% to 5 wt% is similar to that tendency previously reported [41]. In a previous study [41], we have analysed the thermal diffusivity of two sets of PureTemp 8 based nanofluids, one containing MgO nanoparticles and the other containing graphene nanoplatelets. Improvements of 6.5% were achieved for MgO/PureTemp 8 at 5 wt% whilst enhancements up to 32% were found for graphene nanoplatelets/PureTemp 8 at 1 wt%. It is noteworthy that dispersions using the same nanoparticles type, i.e. MgO/PureTemp 8 [41] and here reported MgO/n-C$_{14}$ nanofluids sets, show similar thermal diffusivity enhancements. Likewise, higher improvements are obtained when graphene nanoplatelets are used as nanoadditive. As an example, enhancements in thermal diffusivity up to ~7 or ~4.5 times higher were found when graphene nanoplatelets are dispersed within PureTemp 8 [41] and PEG400 [82], respectively.

4. New understanding on transport properties of nanofluids

As above-mentioned, Andrade [24] presented a theory of the viscosity of liquids from the point of view of solid state instead of from the kinetic theory of gases, stating that the main difference between solid and liquid is the amplitude of molecular motion. Assuming these considerations, it was argued that the viscosity of a liquid surrounding the melting point can be calculated only from experimental constants [24]. At this temperature, there is a communication of momentum between molecules in adjacent layers due to their vibrations at every extreme libration. Therefore, assuming that the probability that a molecule vibrates along each axis is one third, Andrade derived an expression for the viscosity, η, at the melting point, as follows,

$$\eta = \frac{4}{3}\frac{\nu m}{\sigma} \tag{18}$$

where ν, m, and σ stand for the vibration frequency, the mass of the liquid and the average distance between the centre of the molecules, respectively.

On the other hand, Osida [27] developed a model for the thermal conductivity of liquids, assuming that heat is exchanged when translational and rotational energy is transferred due to molecular collisions under a temperature gradient. Considering θ as the angle between the direction of the motion and that of the heat flow (z-axis) and neglecting the internal energy of the molecules, it is easy to assume every molecule has six degrees of freedom and, therefore, its mean energy is $3kT$, where k is Boltzmann's constant. The amount of energy transported when the molecule is vibrating between the hotter and the colder sides is the following:

$$6k\frac{dT}{dz}\sigma\cos(\theta)\nu \tag{19}$$

Let consider a unit cross-area tube in the direction of the heat flow and three normal planes in the tube $z = 0$, $z = l$, $z = l + dl$, with $l \le \sigma$. Multiplying this last result by the amount of molecules crossing the plane $z = 0$ and integrating with respect to θ and l:

$$\int_0^{\arccos\left(\frac{l}{\sigma}\right)}\int_{-\sigma}^{\sigma} 6k\frac{dT}{dz}\sigma\cos(\theta)\nu\,\frac{\sin(\theta)}{\sigma^3}\,dl\,d\theta = \frac{4k\nu}{\sigma}\frac{dT}{dz} \tag{20}$$

Applying the Fourier's law, this result may be equal to $\lambda\cdot\nabla T$, thus,

$$\lambda = \frac{4k\nu}{\sigma} \tag{21}$$

Based on these previous studies by Andrade [24] and Osida [27], Mohanty [28] proposed a simple relationship between the viscosity and the thermal conductivity, derived from Eqs. (18) and (21),

$$\frac{m\lambda}{\eta} = 3k \tag{22}$$

Multiplying by the Avogadro's number N,

$$\frac{M\lambda}{\eta} = 3Nk \tag{23}$$

in which $M = N\cdot m$ is the molecular weight of the liquid. From Eq. 23, Mohanty derived the following relationship based on the observation of experimental data of thermal conductivity and viscosity of some liquids,

$$\frac{M\lambda}{\eta} = \text{constant} \tag{24}$$

Tomida et al. figured out that this relationship actually does not hold constant, but decreased with increasing M and they have empirically found two different dependences for a set of n-alkanes and ionic liquids [29].

Taking into account the particular case of nanofluids (biphasic systems consisting on nanoscale materials dispersed into a fluid), and after pursued several attempts, here we introduce a new and useful relationship between their transport properties, formulating in this way:
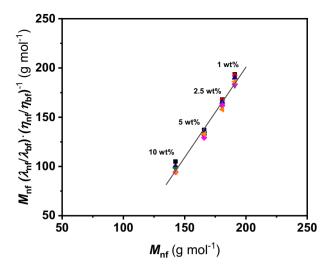
$$M_{nf}\left(\frac{\lambda_{nf}}{\lambda_{bf}}\right)\left(\frac{\eta_{nf}}{\eta_{bf}}\right)^{-1} = AM_{nf} - B \tag{25}$$

where M_{nf} is the molecular weight of the nanofluids,

$$M_{nf} = x_{np}M_{np} + (1 - x_{np})M_{bf} \tag{26}$$

in which x stands for the molar fraction and the subscripts nf, np and bf refer to nanofluid, nanoparticles and base fluid, respectively. The left-term of Eq. 25 which balances the enhancement of the thermal conductivity against the penalty of the increase of viscosity will be hereinafter named as Nanofluid Ratio, NR. Accordingly, the results of this relationship concerning the novel experimental data for the MgO/n-C$_{14}$ nanostructured fluids are presented in Fig. 10. In these dispersions, M_{nf} decreases with nanoparticle molar fraction, x_{np} (or nanoparticle mass fraction, ϕ_m), due to $M_{MgO} < M_{n-C14}$. Indeed, this figure shows the NR as a function of M_{nf}, in which every single point corresponds to a nanofluid at a given temperature and mass fraction. It is important to highlight that all points lay out a single straight line.

All isotherms fall onto the same straight line agreeing with the fact that augmentation of transport properties of nanostructured fluids is non-temperature dependent, as above reported. Likewise, all studied concentrations (up to 10 wt%) fall also on this linear relationship. As can be seen in Fig. 10, the lower the nanofluid molecular weight, the higher the nanoparticle mass fraction, which entails the lower the NR. This is due to η_{nf}/η_{bf} (Fig. 6c) grows faster than $\lambda_{nf}/\lambda_{bf}$ (Fig. 3c) with increasing nanoparticle mass fraction (or decreasing molecular weight), i.e., the viscosity of the colloidal fluid enlarges greater than the thermal conductivity when the concentration of nanomaterial is higher. Subsequently, data in Fig. 10 was correlated by using the above proposed Eq. 25. The obtained coefficients A and B by means of
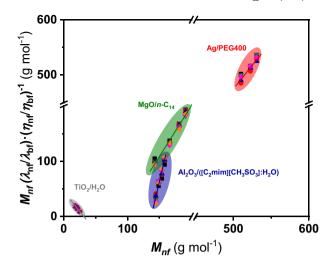
Fig. 10. Nanofluid Ratio as a function of the molecular weight of MgO/n-C$_{14}$ nanostructured fluids at temperatures: 283.15 K (■); 293.15 K (●); 303.15 K (▲); 313.15 K (▼); 323.15 K (◆); and 333.15 K (◀). Linear regression based on Eq. 25 (−).

Fig. 11. Nanofluid Ratio as a function of the molecular weight of Ag/PEG400 [30] (shadowed in red), TiO$_2$/H$_2$O [31] (shadowed in grey), and Al$_2$O$_3$/([C$_2$mim][CH$_3$SO$_3$]:H$_2$O) [32,33] (shadowed in blue), MgO/n-C$_{14}$ (shadowed in green) dispersions at different temperatures: 283.15 K (■); 293.15 K (●); 303.15 K (▲); 313.15 K (▼); 323.15 K (◆); 333.15 K (◀); and 343.15 K (▶). Linear regressions based on Eq. 25 (−). (For interpretation of the references to colour in this figure legend, the reader is referred to the web version of this article.)

a least-squares adjustment are summarized in Table 3 along with the standard deviation and R^2. The goodness of this fitting is well-represented taking into account the coefficient of determination value (0.98), enclosed in Table 3.

With the aim to validate the reliability of this proposed tool, similar analysis based on dispersions literature data of Ag/PEG400 [30], TiO$_2$/H$_2$O [31] and Al$_2$O$_3$/([C$_2$mim][CH$_3$SO$_3$]:H$_2$O) at 0.25 H$_2$O mole fraction [32,33] are presented in Fig. 11. These three nanofluid sets were selected taking into account the available and reliable experimental data in the literature reported by the same laboratory, and to cover a wide variety of base fluids of different chemical nature.

Accordingly, all these dispersions can be adjusted in a similar way as previously described for the here reported MgO/n-C$_{14}$ nanofluids. All isotherms and all studied concentrations fall onto one straight line for each set. It should be highlighted that two different NR trends against M_{nf} can be separated. In fact, Ag/PEG400 and Al$_2$O$_3$/([C$_2$mim][CH$_3$SO$_3$]:H$_2$O) follows the same trend as MgO/n-C$_{14}$, whereas TiO$_2$/H$_2$O just the opposite one, NR always decreasing with increasing nanoadditive mass fraction for all studied nanostructured fluids. This inverse effect is due to ϕ_m and M_{nf} follow a different trend depending on the relation between M_{np} and M_{bf}, according to Eq. 26. Thus, in the cases that fulfil $M_{np} > M_{bf}$ (TiO$_2$/H$_2$O), ϕ_m increases with M_{nf} while the opposite tendency occurs for $M_{np} < M_{bf}$ (MgO/n-C$_{14}$, Ag/PEG400, and Al$_2$O$_3$/([C$_2$mim][CH$_3$SO$_3$]:H$_2$O)). Eq. 25 fits also well these opposite linear trends concerning all analysed literature values (see Table 3), displaying coefficients of determination better or equal to 0.90 for each nanofluid set. The B coefficient, that is positive for nanostructured fluids with $M_{np} < M_{bf}$ while negative for $M_{np} > M_{bf}$, indicates the values of NR at molecular weight equal to 0, so their values are not relevant for any physical analysis purposes.

The above-mentioned trends for $M_{np} < M_{bf}$ correspond to positive A values for all those nanofluid sets in Eq. 25. Properly, A negative value has been obtained for TiO$_2$/H$_2$O, agreeing with $M_{np} > M_{bf}$. A coefficient indicates the variation of the NR with M_{nf}, which is related to the ratio between the enhancement of the thermal conductivity against the penalty of the increase of the viscosity, and the variation of this ratio with nanofluid molecular weight, according to the following equation:

$$A = \frac{\partial NR}{\partial M_{nf}} = \left(\frac{\lambda_{nf}}{\lambda_{bf}}\right)\left(\frac{\eta_{nf}}{\eta_{bf}}\right)^{-1} + M_{nf}\frac{\partial}{\partial M_{nf}}\left[\left(\frac{\lambda_{nf}}{\lambda_{bf}}\right)\left(\frac{\eta_{nf}}{\eta_{bf}}\right)^{-1}\right] \qquad (27)$$

Therefore, the sign of A coefficient is defined by the variation of the ratio between $\lambda_{nf}/\lambda_{bf}$ and η_{nf}/η_{bf} with nanofluid molecular weight, and the different cases for whole possible nanofluids are enclosed in Table 4. A can not be null for any nanofluid and negative A values cannot be also found for those dispersions with $M_{np} < M_{bf}$ while positive A values are neither possible in cases that $M_{np} > M_{bf}$, because the second term in right side of Eq. 27 is always prevalent over the first one. Absolute A values higher than 1 have been obtained in these analyses (Table 3), that entails λ-enhancements to increase lower than its corresponding η-penalty modifications against nanoparticle mass fractions, as can be observed in Table 4. This behaviour agrees with the well-known performance of nanostructured fluids in the literature [30–33,64,65].

Table 3

Temperature and mass fraction ranges, coefficients A and B, 'limit' nanofluid molecular weight, maximum nanoparticle mass fraction, standard deviation, and coefficient of determination of Eq. 25 for MgO/n-C$_{14}$, Ag/PEG400 [30], TiO$_2$/H$_2$O[31], and Al$_2$O$_3$/([C$_2$mim][CH$_3$SO$_3$]:H$_2$O) [32,33] nanofluids.

	MgO/n-C$_{14}$	Ag/PEG400	TiO$_2$/H$_2$O	Al$_2$O$_3$/([C$_2$mim][CH$_3$SO$_3$]:H$_2$O)
T range / K	283.15–333.15	283.15–323.15	293.15–343.15	283.15–333.15
ϕ_m range	0.01–0.10	0.001–0.0114	0.01–0.35	0.01–0.15
A	1.83 ± 0.06	1.71 ± 0.16	−1.44 ± 0.06	4.88 ± 0.23
B / g mol^{-1}	165.51	380.21	−45.36	668.39
$M_{nf,0}$ / g mol^{-1}	90.38	221.81	31.53	136.97
$\phi_{m,0}$	0.31	0.36	0.55	0.39
s / g mol^{-1}	5.4	5.4	0.68	5.9
R^2	0.98	0.90	0.97	0.95

Table 4
Possible scenarios for nanostructured fluids depending on A values from Eq. 25.

	M dependence on A		ϕ_m dependence on A		$\frac{\partial}{\partial M}\left(\frac{\lambda_{nf}/\lambda_{bf}}{\eta_{nf}/\eta_{bf}}\right)$		λ-enhancement vs. η-penalty variation
	$M_{np} < M_{bf}$	$M_{np} > M_{bf}$	$M_{np} < M_{bf}$	$M_{np} > M_{bf}$	$M_{np} < M_{bf}$	$M_{np} > M_{bf}$	
$0 < \lvert A \rvert < 1$					> 0	< 0	$\frac{\partial(\lambda_{nf}/\lambda_{bf})}{\partial\phi_m} > \frac{\partial(\eta_{nf}/\eta_{bf})}{\partial\phi_m}$
$\lvert A \rvert = 1$	↑	↓	↓	↑	0	0	$\frac{\lambda_{nf}}{\lambda_{bf}} = \frac{\eta_{nf}}{\eta_{bf}}, \forall\phi_m$
$\lvert A \rvert > 1$					> 0	< 0	$\frac{\partial(\lambda_{nf}/\lambda_{bf})}{\partial\phi_m} < \frac{\partial(\eta_{nf}/\eta_{bf})}{\partial\phi_m}$

Table 4 also encloses the implications of the other possible scenarios for $\lvert A \rvert \leq 1$. Identical λ-enhancements and η-penalties involves A coefficient equal to 1 whereas $\lvert A \rvert < 1$ infers the ideal conditions for nanofluids from the heat transfer point of view in which increasing concentration loading causes the thermal conductivity enhancement to grow faster than the viscosity penalty. As above indicated, these different outlines also depend on the two possible relations between M_{np} and M_{bf}.

All the analysed nanofluid sets have similar absolute values of A higher than 1 (Table 3) excepting that obtained for Al$_2$O$_3$/([C$_2$mim] [CH$_3$SO$_3$]:H$_2$O) nanodispersions. According to the relationship here proposed, this set would be the less worth as advanced material from heat transfer application perspectives. This can be due to the chemical structure of the ionic liquid, IL, that favours the stabilization of nanoparticles within it [32], fostering superior growing of η_{nf}/η_{bf} ratio than the other considered dispersions, that triggers a higher absolute A value.

The x-intercepts in the linear correlations gathered in Figs. 10 and 11 allow to identify a molecular weight for each nanofluid set that may be associated as a 'limit' nanofluid molecular weight, $M_{nf,0}$, (or the corresponding maximum nanoparticle mass fraction, $\phi_{m,max}$). This point could indicate the hypothetical nanoparticle loading from which the nanodispersion type behaves as a solid according to this proposed relationship. In this sense, we must mention that Eq. 25 is only applicable under the assumption of Newtonian nanofluids throughout the entire considered nanoparticle mass fraction range. Table 5 sums up these limit nanofluid molecular weights, $M_{nf,0}$ and their corresponding maximum nanoparticle mass fraction, $\phi_{m,max}$, for all nanostructured fluid sets. This parameter could be a practical tool when designing nanofluids focused on heat transfer applications, offering a possible estimation of the available nanoparticle mass fraction ranges. Maximum nanoadditive mass fraction values of 31, 36, 39, and 55 wt% are obtained for MgO/n-C$_{14}$, Ag/PEG400, Al$_2$O$_3$/([C$_2$mim][CH$_3$SO$_3$]:H$_2$O), and TiO$_2$/H$_2$O nanostructured fluids, respectively. Although the highest $\phi_{m,max}$ value corresponds to the nanofluid set, TiO$_2$/H$_2$O, with the lowest $\lvert A \rvert$ value, it is also noteworthy that no relation was revealed between $M_{nf,0}$ (or $\phi_{m,max}$) and the molecular weights of the base fluid and/or the nanomaterial.

The presented analysis constitutes an approach that intend to contribute on the designing of nanodispersions for thermal energy applications and from their transport properties point of view in particular. Further developments should be incorporated with the significant support of theoretical and/or numerical studies.

5. Conclusions

This study encloses a thorough analysis and characterization of the thermophysical profile of novel nanofluids based on MgO nanoparticles dispersed within n-C$_{14}$ for their use in cold thermal energy storage applications under a wide nanoparticle loading and temperature ranges along with the proposal of a new empirical relationship of the relevant transport properties of nanofluids to assess their potential use in heat transfer applications.

Good stability of MgO/n-C$_{14}$ nanostructured fluids was reported in static and shaken conditions during 30 days. The thermal conductivity enhances with mass fraction up to 17% for MgO/n-C$_{14}$ at 10 wt% with non-temperature dependence of these enhancements. The goodness

of several models to predict or correlate our experimental data was checked, obtaining AADs% of 6.1%, 6.0%, and 3.1%, for Maxwell, Bruggeman, and Xue predictive equations, respectively, Yamada and Ota correlation showing the lowest AAD%, 0.74%. We found out Newtonian behaviour for all studied nanofluids and conditions, MgO nanoparticles leading the fluids to higher viscosities up to 68% at mass fraction of 10 wt%. The density of nanofluids slightly increase with mass fraction up to 4.5% at 5 wt%, while the isobaric heat capacity experiences a reduction when increasing the mass fraction of dispersed nanoparticles of up to 6%. Finally, the thermal diffusivity increases for all studied mass fractions, up to 13%.

A new relationship was proposed in terms of the balance between the enhancement of the thermal conductivity and the penalty of the increase of viscosity for nanodispersions, based on the theories of Andrade, Osida and Mohanty. The relationship lets describe the mentioned transport properties for a given nanofluid set, i.e., all isotherms and all concentrations, with a single straight line. The reliability of this proposed relationship has been assessed for MgO/n-C$_{14}$ samples as well as for Ag/PEG400, TiO$_2$/H$_2$O, and Al$_2$O$_3$/([C$_2$mim][CH$_3$SO$_3$]:H$_2$O) nanofluid sets, obtaining coefficients of determination higher than 0.90. Similar trends have been found for all sets excepting TiO$_2$/H$_2$O, this differentiated behaviour being expected by this new relationship. Contributions from theoretical and numerical works should be incorporated to complete this first approach on understanding the enhancing mechanism of nanofluids. However, the reported results evidences that this proposal offers an advanced understanding of transport properties of nanofluids with respect to the stablished literature and an interesting innovative tool to design new nanostructured fluids for heat transfer applications.

Declaration of Competing Interest

Authors declare no conflict of interest.

Acknowledgments

References

[1] L. Meyer, S. Brinkman, L. van Kesteren, N. Leprince-Ringuet, F. van Boxmeer, IPCC, 2014: climate change 2014: synthesis report. Contribution of working groups I, II and III to the fifth assessment report of the intergovernmental panel on climate change, in: R.K. Pachauri, L.A. Meyer (Eds.), The Intergovernmental Panel on Climate Change (IPCC), United Nations, Geneva, Switzerland 2014, pp. 3–87.

[2] V. Dobravec, N. Matak, C. Sakulin, G. Krajačić, Multilevel governance energy planning and policy: a view on local energy initiatives, Ener. Sustain. Soc. 11 (2021) 2, https://doi.org/10.1186/s13705-020-00277-y.

[3] J. Rogelj, M. den Elzen, N. Höhne, T. Fransen, H. Fekete, H. Winkler, R. Schaeffer, F. Sha, K. Riahi, M. Meinshausen, Paris agreement climate proposals need a boost to keep warming well below 2°C, Nature 534 (2016) 631–639, https://doi.org/10.1038/nature18307.

[4] J. Rogelj, O. Fricko, M. Meinshausen, V. Krey, J.J.J. Zilliacus, K. Riahi, Understanding the origin of Paris agreement emission uncertainties, Nat. Commun. 8 (2017) 15748, https://doi.org/10.1038/ncomms15748.

[5] A. Grubler, C. Wilson, N. Bento, B. Boza-Kiss, V. Krey, D.L. McCollum, N.D. Rao, K. Riahi, J. Rogelj, S. De Stercke, J. Cullen, S. Frank, O. Fricko, F. Guo, M. Gidden, P. Havlík, D. Huppmann, G. Kiesewetter, P. Rafaj, W. Schoepp, H. Valin, A low energy demand scenario for meeting the 1.5°C target and sustainable development goals without negative emission technologies, Nat. Energy 3 (2018) 515–527, https://doi.org/10.1038/s41560-018-0172-6.

[6] Directive 2010/31/EU of the European Parliament and of the Council of 19 May 2010 on the Energy Performance of Buildings. , European Union, 2010.

[7] Mapping and Analyses of the Current and Future (2020−2030) Heating/Cooling Fuel Deployment (Fossil/Renewables). , European Commission, 2016.

[8] X. Xu, X. Zhang, J.M. Munyalo, Key technologies and research progress on enhanced characteristics of cold thermal energy storage, J. Mol. Liq. 278 (2019) 428–437, https://doi.org/10.1016/j.molliq.2019.01.040.

[9] G. Alva, Y. Lin, G. Fang, An overview of thermal energy storage systems, Energy 144 (2018) 341–378, https://doi.org/10.1016/j.energy.2017.12.037.

[10] G. Li, Y. Hwang, R. Radermacher, Review of cold storage materials for air conditioning application, Int. J. Refrig. 35 (2012) 2053–2077, https://doi.org/10.1016/j.ijrefrig.2012.06.003.

[11] N.V. Plechkova, K.R. Seddon, Applications of ionic liquids in the chemical industry, Chem. Soc. Rev. 37 (2008) 123–150, https://doi.org/10.1039/B006677J.

[12] H.M. Ali, Recent advancements in PV cooling and efficiency enhancement integrating phase change materials based systems – a comprehensive review, Sol. Energy 197 (2020) 163–198, https://doi.org/10.1016/j.solener.2019.11.075.

[13] Z. Chen, A. Shahsavar, A.A.A.A. Al-Rashed, M. Afrand, The impact of sonication and stirring durations on the thermal conductivity of alumina-liquid paraffin nanofluid: an experimental assessment, Powder Technol. 360 (2020) 1134–1142, https://doi.org/10.1016/j.powtec.2019.11.036.

[14] N. Sezer, M.A. Atieh, M. Koç, A comprehensive review on synthesis, stability, thermophysical properties, and characterization of nanofluids, Powder Technol. 344 (2019) 404–431, https://doi.org/10.1016/j.powtec.2018.12.016.

[15] Y. Hong, S. Ding, W. Wu, J. Hu, A.A. Voevodin, E. Snyder, L. Chow, M. Su, Enhancing heat capacity of colloidal suspension using nanoscale encapsulated phase-change materials for heat transfer, ACS Appl. Mater. Interfaces 2 (2010) 1685–1691, https://doi.org/10.1021/am100204b.

[16] N.S. Bondareva, B. Buonomo, O. Manca, M.A. Sheremet, Heat transfer performance of the finned nano-enhanced phase change material system under the inclination influence, Int. J. Heat Mass Transf. 135 (2019) 1063–1072, https://doi.org/10.1016/j.ijheatmasstransfer.2019.02.045.

[17] H.M. Ali, Analysis of heat pipe-aided graphene-oxide based nanoparticle-enhanced phase change material heat sink for passive cooling of electronic components, J. Therm. Anal. Calorim. 146 (2021) 277–286, https://doi.org/10.1007/s10973-020-09946-8.

[18] A. Asadi, S. Aberoumand, A. Moradikazerouni, F. Pourfattah, G. Żyła, P. Estellé, O. Mahian, S. Wongwises, H.M. Nguyen, A. Arabkoohsar, Recent advances in preparation methods and thermophysical properties of oil-based nanofluids: a state-of-the-art review, Powder Technol. 352 (2019) 209–226, https://doi.org/10.1016/j.powtec.2019.04.054.

[19] H. Jiang, Q. Xu, C. Huang, L. Shi, Effect of temperature on the effective thermal conductivity of n-tetradecane-based nanofluids containing copper nanoparticles, Particuology 22 (2015) 95–99, https://doi.org/10.1016/j.partic.2014.10.010.

[20] J.D.V.D. Waals, On the Theory of the Friction of Liquids, XXI, Proc. Kon. Ned. Akad. Wetensch, 1919 743–755.

[21] J.D.V.D. Waals, On the theory of the friction of liquids, II, Proc. Kon. Ned. Akad. Wetensch, XXI, 1919, pp. 1283–1293.

[22] L. Brillouin, La viscosité des liquides et son interprétation théorique, J Phys Radium 3 (1922) 326–340.

[23] P.W. Bridgman, The Physics of High Pressure, G. Bell and sons, Limited, 1931.

[24] E.N.D.C. Andrade, A theory of the viscosity of liquids.—part I, Lond. Edinb. Dubl. Phil. Mag. 17 (1934) 497–511, https://doi.org/10.1080/14786443409462409.

[25] P. Debye, Polar molecules, Dover Publications, New York, 1929.

[26] F.A. Lindemann, Über die Berechnung Molekularer Eigenfrequenzen, Phys. Z. 11 (1910) 609–612.

[27] I. Osida, On the thermal conductivity of liquid, Proc Phys Math Soc Jpn 21 (1939) 353–356, https://doi.org/10.11429/ppmsj1919.21.6_353.

[28] S.R. Mohanty, A relationship between heat conductivity and viscosity of liquids, Nature 168 (1951) 42, https://doi.org/10.1038/168042a0.

[29] D. Tomida, S. Kenmochi, T. Tsukada, K. Qiao, C. Yokoyama, Thermal conductivities of [bmim][PF6], [hmim][PF6], and [omim][PF6] from 294 to 335 K at pressures up to 20 MPa, Int. J. Thermophys. 28 (2007) 1147–1160, https://doi.org/10.1007/s10765-007-0241-8.

[30] M.A. Marcos, D. Cabaleiro, S. Hamze, L. Fedele, S. Bobbo, P. Estellé, L. Lugo, NePCM based on silver dispersions in poly(ethylene glycol) as a stable solution for thermal storage, Nanomaterials 10 (2020) 19.

[31] L. Fedele, L. Colla, S. Bobbo, Viscosity and thermal conductivity measurements of water-based nanofluids containing titanium oxide nanoparticles, Int. J. Refrig. 35 (2012) 1359–1366, https://doi.org/10.1016/j.ijrefrig.2012.03.012.

[32] E.I. Cherecheş, J.I. Prado, M. Cherecheş, A.A. Minea, L. Lugo, Experimental study on thermophysical properties of alumina nanoparticle enhanced ionic liquids, J. Mol. Liq. 291 (2019) 111332https://doi.org/10.1016/j.molliq.2019.111332.

[33] E.I. Cherecheş, J.I. Prado, C. Ibanescu, M. Danu, A.A. Minea, L. Lugo, Viscosity and isobaric specific heat capacity of alumina nanoparticle enhanced ionic liquids: an experimental approach, J. Mol. Liq. 317 (2020) 114020https://doi.org/10.1016/j.molliq.2020.114020.

[34] W.M. Haynes, D.R. Lide, CRC Handbook of Chemistry and Physics: A Ready-Reference Book of Chemical and Physical Data, 92th ed CRC Press, Boca Raton, 2011.

[35] C.-C. Li, M.-H. Chang, Colloidal stability of CuO nanoparticles in alkanes via oleate modifications, Mater. Lett. 58 (2004) 3903–3907, https://doi.org/10.1016/j.matlet.2004.05.088.

[36] L. Fedele, L. Colla, S. Bobbo, S. Barison, F. Agresti, Experimental stability analysis of different water-based nanofluids, Nanoscale Res. Lett. 6 (2011) 300, https://doi.org/10.1186/1556-276X-6-300.

[37] C.A. Nieto de Castro, B. Taxis, H.M. Roder, W.A. Wakeham, Thermal diffusivity measurement by the transient hot-wire technique: a reappraisal, Int. J. Thermophys. 9 (1988) 293–316, https://doi.org/10.1007/BF00513073.

[38] D. Cabaleiro, M.J. Pastoriza-Gallego, C. Gracia-Fernández, M.M. Piñeiro, L. Lugo, Rheological and volumetric properties of TiO2-ethylene glycol nanofluids, Nanoscale Res. Lett. 8 (2013)https://doi.org/10.1186/1556-276X-8-286.

[39] W. Wagner, A. Pruß, The IAPWS formulation 1995 For the thermodynamic properties of ordinary water substance for general and scientific use, J. Phys. Chem. Ref. Data, 31 (2002) 387–535. https://doi.org/10.1063/1.1461829.

[40] M.O. McLinden, J.D. Splett, A liquid density standard over wide ranges of temperature and pressure based on toluene, J Res Natl Inst Stand Technol 113 (2008) 29–67.

[41] J.I. Prado, L. Lugo, Enhancing the thermal performance of a stearate phase change material with graphene nanoplatelets and MgO nanoparticles, ACS Appl. Mater. Interfaces 12 (2020) 39108–39117, https://doi.org/10.1021/acsami.0c09643.

[42] D. Cabaleiro, C. Gracia-Fernández, J.L. Legido, L. Lugo, Specific heat of metal oxide nanofluids at high concentrations for heat transfer, Int. J. Heat Mass Transf. 88 (2015) 872–879, https://doi.org/10.1016/j.ijheatmasstransfer.2015.04.107.

[43] D. Cabaleiro, C. Gracia-Fernández, L. Lugo, (Solid+liquid) phase equilibria and heat capacity of (diphenyl ether+biphenyl) mixtures used as thermal energy storage materials, J. Chem. Thermodyn. 74 (2014) 43–50, https://doi.org/10.1016/j.jct.2014.03.029.

[44] N.W. Song, K.M. Park, I.H. Lee, H. Huh, Uncertainty estimation of nanoparticle size distribution from a finite number of data obtained by microscopic analysis, Metrologia 46 (2009) 480–488, https://doi.org/10.1088/0026-1394/46/5/012.

[45] M. Klinger, A. Jäger, Crystallographic tool box (CrysTBox): automated tools for transmission electron microscopists and crystallographers, J. Appl. Crystallogr. 48 (2015) 2012–2018, https://doi.org/10.1107/S1600576715017252.

[46] V. Harnchana, A.P. Brown, R.M. Brydson, J.P. Harrington, A.T. Hindmarch, C.H. Marrows, B.J. Hickey, TEM characterization of a magnetic tunnel junction, J. Phys. Conf. Ser. 126 (2008) 012058https://doi.org/10.1088/1742-6596/126/1/012058.

[47] J. Nuncira, L.M. Seara, R.D. Sinisterra, V. Caliman, G.G. Silva, Long-term colloidal stability of graphene oxide aqueous nanofluids, Fuller Nanotub Car N 28 (2020) 407–417, https://doi.org/10.1080/1536383X.2019.1695250.

[48] J.C.G. Calado, J.M.N.A. Fareleira, C.A. Nieto de Castro, W.A. Wakeham, Thermal conductivity of five hydrocarbons along the saturation line, Int. J. Thermophys. 4 (1983) 193–208, https://doi.org/10.1007/BF00502352.

[49] Y. Wada, Y. Nagasaka, A. Nagashima, Measurements and correlation of the thermal conductivity of liquid n-paraffin hydrocarbons and their binary and ternary mixtures, Int. J. Thermophys. 6 (1985) 251–265, https://doi.org/10.1007/BF00522147.

[50] M.M. Kenisarin, Thermophysical properties of some organic phase change materials for latent heat storage. A review, Sol. Energy 107 (2014) 553–575, https://doi.org/10.1016/j.solener.2014.05.001.

[51] J.C. Maxwell, A Treatise on Electricity and Magnetism, Clarendon press, 1881.

[52] D.A.G. Bruggeman, Berechnung Verschiedener Physikalischer Konstanten von Heterogenen Sustanzen. I. Dielektrizitätskonstanten und Leitfähigkeiten der Mischkörper aus Isotropen Substanzen, Ann. Phys. 24 (1935) 636–679.

[53] Q.Z. Xue, Model for thermal conductivity of carbon nanotube-based composites, Physica B 368 (2005) 302–307, https://doi.org/10.1016/j.physb.2005.07.024.

[54] E. Yamada, T. Ota, Effective thermal conductivity of dispersed materials, Heat Mass Transf. 13 (1980) 27–37, https://doi.org/10.1007/BF00997630.

[55] A.M. Hofmeister, Thermal diffusivity and thermal conductivity of single-crystal MgO and Al2O3 and related compounds as a function of temperature, Phys. Chem. Miner. 41 (2014) 361–371, https://doi.org/10.1007/s00269-014-0655-3.

[56] S.M.S. Murshed, K.C. Leong, C. Yang, Enhanced thermal conductivity of TiO2-water based nanofluids, Int. J. Therm. Sci. 44 (2005) 367–373, https://doi.org/10.1016/j.ijthermalsci.2004.12.005.

[57] A.K. Sharma, A.K. Tiwari, A.R. Dixit, Rheological behaviour of nanofluids: a review, Renew. Sust. Energ. Rev. 53 (2016) 779–791, https://doi.org/10.1016/j.rser.2015.09.033.

[58] D. Ducoulombier, H. Zhou, C. Boned, J. Peyrelasse, H. Saint-Guirons, P. Xans, Pressure (1-1000 bars) and temperature (20-100 °C) dependence of the viscosity of liquid hydrocarbons, J. Phys. Chem. 90 (1986) 1692–1700, https://doi.org/10.1021/j100399a047.

[59] L. Zhang, Y. Guo, H. Wei, F. Yang, W. Fang, R. Lin, Densities and viscosities of binary mixtures of exo-tetrahydrodicyclopentadiene with n-undecane or n-tetradecane at T = (293.15 to 313.15) K, J. Chem. Eng. Data 55 (2010) 4108–4113, https://doi.org/10.1021/je100313a.

[60] H. Liu, L. Zhu, Excess molar volumes and viscosities of binary systems of butylcyclohexane with n-alkanes (C7 to C14) at T = 293.15 K to 313.15 K, J. Chem. Eng. Data 59 (2014) 369–375, https://doi.org/10.1021/je400835u.

J.I. Prado, J.P. Vallejo and L. Lugo

Powder Technology 397 (2022) 117082

[61] D.J. Luning Prak, B.G. Lee, J.S. Cowart, P.C. Trulove, Density, viscosity, speed of sound, bulk modulus, surface tension, and flash point of binary mixtures of butylbenzene + linear alkanes (*n*-decane, *n*-dodecane, *n*-tetradecane, *n*-hexadecane, or *n*-heptadecane) at 0.1 MPa, J. Chem. Eng. Data 62 (2017) 169–187, https://doi.org/10.1021/acs.jced.6b00542.

[62] T.V.M. Santos, M.F.V. Pereira, H.M.N.T. Avelino, F.J.P. Caetano, J.M.N.A. Fareleira, Viscosity and density measurements on liquid *n*-tetradecane at moderately high pressures, Fluid Phase Equilib. 453 (2017) 46–57, https://doi.org/10.1016/j.fluid.2017.08.025.

[63] K. Kian, A.M. Scurto, Viscosity of compressed CO_2-saturated *n*-akanes: CO_2/n-hexane, CO_2/n-decane, and CO_2/n-tetradecane, J. Supercrit. Fluids 133 (2018) 411–420, https://doi.org/10.1016/j.supflu.2017.10.030.

[64] D. Cabaleiro, L. Colla, S. Barison, L. Lugo, L. Fedele, S. Bobbo, Heat transfer capability of (ethylene glycol + water)-based nanofluids containing graphene nanoplatelets: design and thermophysical profile, Nanoscale Res. Lett. 12 (2017) 53, https://doi.org/10.1186/s11671-016-1806-x.

[65] G. Żyła, Viscosity and thermal conductivity of MgO–EG nanofluids, J. Therm. Anal. Calorim. 129 (2017) 171–180, https://doi.org/10.1007/s10973-017-6130-x.

[66] J.P. Vallejo, J. Pérez-Tavernier, D. Cabaleiro, J. Fernández-Seara, L. Lugo, Potential heat transfer enhancement of functionalized graphene nanoplatelet dispersions in a propylene glycol-water mixture. Thermophysical profile, J. Chem. Thermodyn. 123 (2018) 174–184, https://doi.org/10.1016/j.jct.2018.04.007.

[67] H. Vogel, Das Temperature-Unabhängigkeitsgesetz der Viskosität von Flüssigkeiten, Phys. Z. 23 (1922) 645–646.

[68] G.S. Fulcher, Analysis of recent measurements of the viscosity of glasses, J. Am. Ceram. Soc. 8 (1925) 339–355, https://doi.org/10.1111/j.1151-2916.1925.tb16731.x.

[69] G. Tammann, W. Hesse, Die Abhängigkeit der Viscosität von der Temperatur bie Unterkühlten Flüssigkeiten, Z. Anorg. Allg. Chem. 156 (1926) 245–257, https://doi.org/10.1002/zaac.19261560121.

[70] R. Levit, J.C. Martinez-Garcia, D.A. Ochoa, J.E. García, The generalized Vogel-Fulcher-Tamman equation for describing the dynamics of relaxor ferroelectrics, Sci. Rep. 9 (2019) 12390, https://doi.org/10.1038/s41598-019-48864-0.

[71] D.L. Camin, F.D. Rossini, Physical properties of 14 American petroleum institute research hydrocarbons, C9 to C15, J. Phys. Chem. 59 (1955) 1173–1179.

[72] A. Johansen, Density of hydrocarbons in liquid state as a function of temperature, Phys-Chem. Prop. Individ. Hydrocarbons (1960) 85–112.

[73] T.S. Khasanshin, A.P. Shchemelev, The thermodynamic properties of *n*-tetradecane in liquid state, High Temp. 40 (2002) 207–211, https://doi.org/10.1023/A:1015247021970.

[74] J.L. Valencia, D. González-Salgado, J. Troncoso, J. Peleteiro, E. Carballo, L. Romaní, Thermophysical characterization of liquids using precise density and isobaric heat capacity measurements as a function of pressure, J. Chem. Eng. Data 54 (2009) 904–915, https://doi.org/10.1021/je8006875.

[75] M. Kariznovi, H. Nourozieh, J.G. Guan, J. Abedi, Measurement and modeling of density and viscosity for mixtures of athabasca bitumen and heavy *n*-alkane, Fuel 112 (2013) 83–95, https://doi.org/10.1016/j.fuel.2013.04.071.

[76] B.C. Pak, Y.I. Cho, Hydrodynamic and heat transfer study of dispersed fluids with submicron metallic oxide particles, Exp Heat Transf 11 (1998) 151–170, https://doi.org/10.1080/08916159808946559.

[77] M.A. Marcos, N.E. Podolsky, D. Cabaleiro, L. Lugo, A.O. Zakharov, V.N. Postnov, N.A. Charykov, S.V. Ageev, K.N. Semenov, MWCNT in PEG-400 nanofluids for thermal applications: a chemical, physical and thermal approach, J. Mol. Liq. 294 (2019), 111616https://doi.org/10.1016/j.molliq.2019.111616.

[78] M.S. Benson, P.S. Snyder, J. Winnick, Heat capacities of liquid *n*-alkanes at elevated pressures, J. Chem. Thermodyn. 3 (1971) 891–898, https://doi.org/10.1016/S0021-9614(71)80019-8.

[79] J.M. Pardo, C.A. Tovar, D. González, E. Carballo, L. Romaní, Thermophysical properties of the binary mixtures diethyl carbonate + (*n*-dodecane or *n*-tetradecane) at several temperatures, J. Chem. Eng. Data 46 (2001) 212–216, https://doi.org/10.1021/je000197a.

[80] T. Regueira, F. Varzandeh, E.H. Stenby, W. Yan, Heat capacity and joule-Thomson coefficient of selected *n*-alkanes at 0.1 and 10 MPa in broad temperature ranges, J. Chem. Thermodyn. 111 (2017) 250–264, https://doi.org/10.1016/j.jct.2017.03.034.

[81] R. Raud, B. Hosterman, A. Diana, T.A. Steinberg, G. Will, Experimental study of the interactivity, specific heat, and latent heat of fusion of water based nanofluids, Appl. Therm. Eng. 117 (2017) 164–168, https://doi.org/10.1016/j.applthermaleng.2017.02.033.

[82] M.A. Marcos, D. Cabaleiro, M.J.G. Guimarey, M.J.P. Comuñas, L. Fedele, J. Fernández, L. Lugo, PEG 400-based phase change materials nano-enhanced with functionalized graphene nanoplatelets, Nanomaterials 8 (2018) 16, https://doi.org/10.3390/nano8010016.